nature communications

Article

https://doi.org/10.1038/s41467-026-69434-9

Dynamic photochromism in cocrystals and tri-state fluorescence switching in films for multilevel optical encryption

Received: 11 September 2025

Accepted: 2 February 2026

Published online: 10 February 2026

Check for updates

Shuzhen Li ✉, Menghao Xing, Xifan Xu, Wenjing Hu, Hang Zhou & Xiaoyu Cao ✉

Organic crystalline systems combining dynamic photosalient effect with static photochromism represent a promising class of intelligent responsive materials. In this work, we construct a 3Abf-Ofn cocrystal (3Abf = 3-aminodibenzofuran, Ofn=Octafluoronaphthalene) through molecular co-assembly strategy. Upon UV irradiation, the 3Abf-Ofn undergoes a solid-state transformation involving volatile Ofn release and N-N coupling of 3Abf to bis(benzofuran-3-yl) azo compound (Bfa), triggering significant photochromism and photosalient behavior. This reaction pathway differs from conventional mechanisms such as photoisomerization or cycloaddition, representing an example of such photochemical process in organic cocrystals. Furthermore, the 3Abf-Ofn@PMMA composite film exhibits dynamically tunable fluorescence under UV irradiation: an initial enhancement of fluorescence upon photoactivation, followed by excitation wavelength-dependent emission (EWDE) and progressive fluorescence quenching, showing great potential for advanced anti-counterfeiting and information encryption applications. This work not only provides valuable insights for designing multifunctional, light-controlled organic luminescent materials but also offers complementary synthetic approaches to azo-aromatic compounds.

Photo-responsive dynamic materials, capable of exhibiting various macroscopic mechanical effects (such as bending, twisting, rotating, jumping, expanding, and fragmentation) in response to light stimuli, have received widespread attention in the fields of soft robotics, flexible electronics, sensors, and actuators[1–5]. In particular, light as a non-contact stimulus source possesses inherent advantages of cleanliness, adjustability in real time, and high precision, presenting a promising opportunity for the further development of intelligent photomechanical materials. In addition, compared with polymer-based materials such as hydrogels, rubbers, and liquid crystals[6–8], molecular crystals stand out for their fast response, as well as rapid coupling between light and mechanical energy within the long-range ordered stacking structures, which can be conducive to further elucidating the relationship between structure and photomechanical properties through single crystal X-ray diffraction[9–11]. To date, common dynamic photomechanical molecular crystalline materials have mainly been investigated in light-sensitive chromophore systems (e.g., diarylethenes, azobenzenes, anthracenes, and stilbenes)[12–16]. The mechanical motions of such molecular crystals are predominantly driven by photochemical reactions, including photoisomerization, photocycloaddition, photodimerization, and other photoinduced reactions, thereby releasing accumulated strain energy. Once the strain is above the threshold and isn't canceled, the macroscopic photo-responsive mechanical motions would be observed[17–20]. Currently, many photo-responsive crystalline materials can dynamically respond to light stimuli. However, research on integrating multiple distinguishable output signals for a single material is still relatively limited[14].

In the context of photo-responsive materials, photochromism refers to a phenomenon wherein photosensitive substances undergo

School of Chemistry and Chemical Engineering, Henan University of Technology, Zhengzhou, P. R. China. ✉e-mail: lishuzhen@haut.edu.cn; caoxy@haut.edu.cn

reversible changes in color upon exposure to specific wavelengths of light, driven by structural transformations or electronic transitions, which are distinguished by pronounced color contrast and undetectable fluorescent signals under natural light[21–25]. These materials possess advantages for high-security, diversified, and intelligent information protection, making them as ideal candidates for light-induced static response applications[26–31]. Despite significant research progress and widespread practical applications of organic photochromic materials, the integration of the photochromic process with dynamic mechanical responses in a single system remains a key challenge, possibly attributed to the rational design of multi-channel response modes based on synergistic action mechanisms.

Cocrystals engineering enables precise modulation of molecular conformations, intermolecular interactions, and structural dimensions through rational selection of co-assembled unit (co-former), achieving well-ordered molecular arrangement and spatial stacking at the supramolecular scale, often giving rise to emergent physicochemical properties that go beyond the simple sum of the individual components[32–36]. For example, Michael R. Wasielewski et al. studied the influence of chiral electron acceptors on charge transfer dynamics and triplet exciton formation in charge transfer cocrystals[37]. Tang et al. reported triethylamine vapor induces a cyclization reaction in AOTC cocrystals, accompanied by a cocrystal-to-polycrystal phase transition process, converting the non-emissive fluorescence state of AOTC into a red-emissive ACTC cocrystal and a blue-emissive AIC[38].The structural tunability of cocrystals materials[39–41] make them an ideal platform for exploring light-driven chemical reactions, as their ordered molecular packing can regulate the reactivity, selectivity, and kinetic behavior of photochemical processes effectively. The convergence of crystal engineering and photochemistry is emerging as a promising pathway for developing intelligent photoresponsive materials. Nevertheless, current research on photo-responsive cocrystals remains predominantly focused on classical photochemical processes, such as isomerization or cycloaddition reactions, with limited exploration of diverse reaction pathways and their multifunctional outputs[42]. Therefore, designing co-crystal systems through supramolecular self-assembly to regulate photochemical reactions, and further translating structure changes induced by chemical reactions into tunable functional properties, holds significant scientific importance. Particularly, the synergistic mechanism between guest release in cocrystal and photochemical reactions, and how the cascade process transforms molecular-scale structural evolution into dual optical-mechanical responses, has lacked systematic investigation.

In this work, we present a single organic molecular cocrystal that integrates photosensitive mechanical effect and photochromism, co-assembled from the 3Abf and Ofn building blocks via dominant π-π stacking interactions (Fig. 1). The 3Abf molecule as an electron donor (D) adopts a disordered stacking arrangement, while Ofn, as an electron acceptor (A) satisfies energy matching in the 3Abf-Ofn cocrystal system. Under UV irradiation, photoinduced electron transfer (PET) between 3Abf and Ofn generates cationic radicals, enabling the observation of clear photochromic properties. Concurrently, photoactive 3Abf undergoes a photochemical reaction that rapidly promotes Ofn release, triggering macroscopic mechanical motions by releasing accumulated strain. Single-crystal X-ray data (SCXRD) confirms that Bfa is the final photoproduct, rather than undergoing complex and cumbersome chemical synthesis traditionally required for azobenzene derivatives. Control experiments with structurally related amine donors demonstrate the potential generality of this photochemical N–N coupling strategy. Moreover, the significant photo-induced fluorescence enhancement effect can be achieved by embedding 3Abf-Ofn into PMMA matrix. Subsequently, the fluorescence gradually diminishes, accompanied by progressive photochromic transformation upon continuous 365 nm UV irradiation. The 3Abf-Ofn@PMMA films also present tunable excitation wavelength-dependent emission fluorescence ranging from blue to red light. Thus, this study provides an advanced strategy for constructing multifunctional responsive organic crystalline materials, laying the foundation for their potential applications in optical anti-counterfeiting.

Results

Synthesis and photo-responsive properties of 3Abf-Ofn cocrystal

3Abf-Ofn cocrystals were obtained in 1:1 stoichiometry ratio by slow evaporation from the mixed solvent (methanol: dichloromethane=1:1) at room temperature. The crystalline products present a transparent,

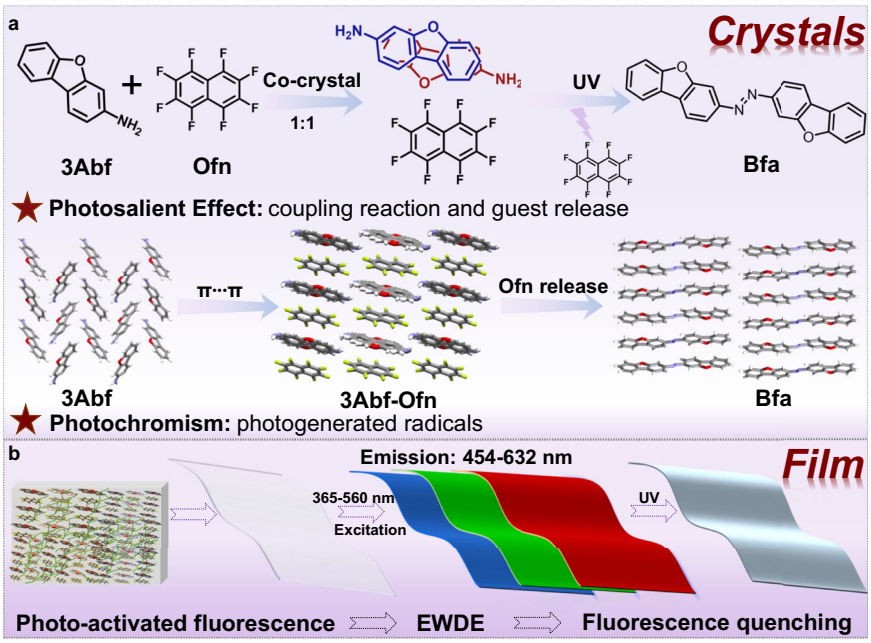

Fig. 1 | Schematic illustration of 3Abf-Ofn cocrystal and 3Abf-Ofn@PMMA film. a Chemical structures and self-assembled patterns of 3-aminodibenzofuran (3Abf), Octafluoronaphthalene (Ofn), 3Abf-Ofn cocrystal and photoproduct bis(benzofuran-3-yl) azo (Bfa). **b** Dynamically tunable fluorescence of 3Abf-Ofn@PMMA film.

https://doi.org/10.1038/s41467-026-69434-9

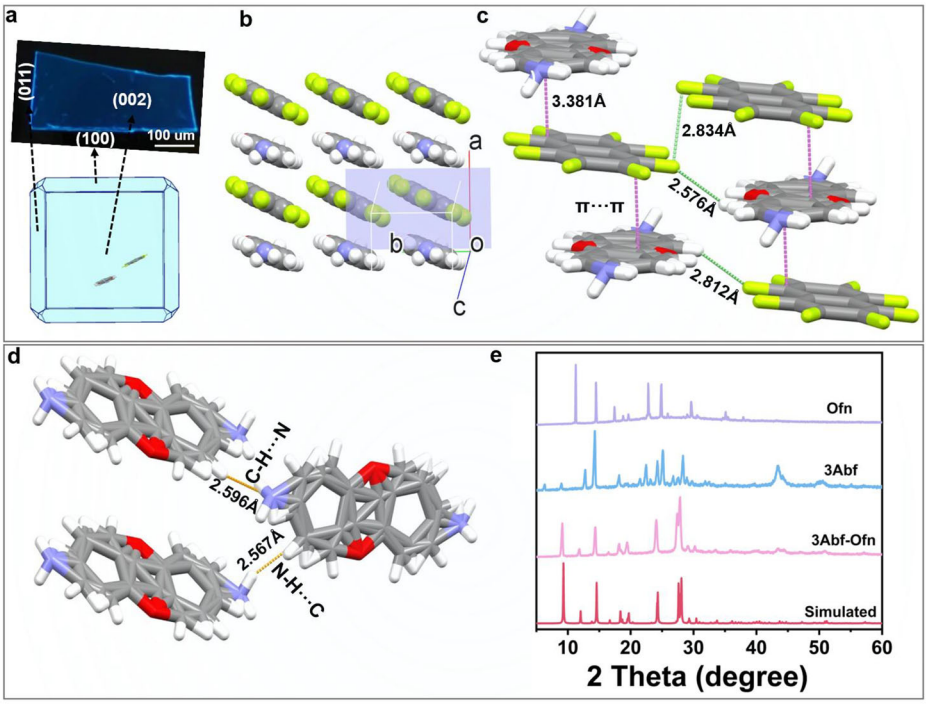

Fig. 2 | Characterization of the cocrystal. a Predicted morphology and corresponding crystal faces of 3Abf-Ofn crystal. **b** Crystal packing structure parallel to the (002) miller plane. **c** Intermolecular π···π, C-H···F and F···F contacts of 3Abf-Ofn cocrystal. **d** Hydrogen bond interactions of 3Abf-Ofn crystal. **e** PXRD patterns of experimental sample and simulated results from single crystal structures of 3Abf-Ofn crystal.

well-defined two-dimensional (2D) plate-like morphology with blue fluorescence, which are consistent with the predicted crystal morphology by Bravais–Friedel Donnay–Harker calculations[22,43] (Fig. 2a). The predicted morphology shows that the largest crystal faces correspond to the (002) miller plane based on the single-crystal structure analysis, which is parallel to the slipped 3Abf–Ofn columnar stacks (Fig. 2b). The crystallographic data of 3Abf-Ofn cocrystal (Supplementary Table 1) show it belongs to a monoclinic system with the centrosymmetric space group of $P2_1/c$ (No.14). Adjacent 3Abf molecules adopt a head-to-tail stacking mode with close overlap and disordered conformations, which may facilitate the susceptibility of the material to internal strain. The disorder of the 3Abf molecule arises from its crystallographic placement at a special position, as the local symmetry of the lattice site is higher than the intrinsic symmetry of the 3Abf molecule, which crystallizes in the orthorhombic $Pna2_1$ space group. Moreover, the ordered Ofn molecules are intercalated between two layers of disordered 3Abf molecules with the larger interlayer spacing distance of 3.381 Å and overlapping area of nearly 95%, forming a mixed stacking structural motif (DADADA) through π − π interactions[41] (Fig. 2c). Such alternating stacks column enhances strong electronic coupling[44], promoting PET from 3Abf to Ofn. In addition, adjacent 3Abf motifs are interconnected via C-H···N and N-H···C hydrogen bonding interactions in a staggered arrangement (Fig. 2d), with the dihedral angle of 40.59° and 42.63° (Supplementary Fig. 1). Likewise, neighboring Ofn molecules are linked by F···F contacts, with no significant interplanar twist between adjacent naphthalene rings (Supplementary Fig. 2). Both molecular components further extend into 2D supramolecular layers infinitely along the *c*-axis (Supplementary Fig. 3). Furthermore, the phase purity and crystalline nature of the as-prepared 3Abf-Ofn during crystallization can be elucidated by powder X-ray diffraction (PXRD) analysis, which show good agreement with the simulated pattern from single-crystal structure, the intense (002) diffraction peak indicates a preferred orientation (Fig. 2e). Fourier transform infrared (FT-IR) spectra indirectly reveals the formation of 3Abf–Ofn cocrystal containing both characteristic vibrational peak of building blocks (Supplementary Fig. 4). Thermogravimetric analysis (TGA) shows the 3Abf-Ofn cocrystal exhibits good thermal stability and remain undecomposed until reaching 145.8 °C (Supplementary Fig. 5), which differs from thermal behavior that of the individual 3Abf and Ofn molecules (Supplementary Fig. 6), further confirming two-component self-assembly strategy can effectively modulate the thermal stability of single-component systems.

As shown in Fig. 3a and Supplementary Movie 1, the obvious static photochromic behavior and dynamic photomechanical effect of macroscopic 3Abf-Ofn crystals can be first observed simultaneously, which are absent in the 3Abf crystals (Supplementary Fig. 7). Upon irradiation with UV light (365 nm, 441 mW/cm^2), the 3Abf-Ofn crystals ($0.15 \times 0.1 \times 0.05$ mm^3) changes from colorless to brown rapidly within 4 s, accompanied by the fading of green fluorescence. Concurrently, the crystals show a distinct photosalient (splitting and jumping) effect in response to UV light. When the duration of light irradiation time range of 0–2 minutes, the 3Abf-Ofn crystals undergo fast and obvious splitting actuation, and break down into individual microcrystals suddenly, some of which jumped to random directions beyond the illuminated area and remain unchanged thereafter, suggesting that such crystalline material exhibits a specific response to UV light. Notably, the micro-sized crystalline fracture surfaces emit bright green fluorescence under UV light, which rapidly diminishes and eventually disappears completely, implying that the high-contrast photochromic transformation of the crystals occurs continuously throughout the entire illumination process. Furthermore, it is observed that the needle-like fragmented crystal retains a curved morphology with an angle of 10.16° without reverting to its original straight shape upon removal of the light source, indicating a certain degree of light-induced plastic deformation (Supplementary Fig. 8). The light-induced mechanical motion and photochromic behavior can also be presented in crystals of different sizes with varying

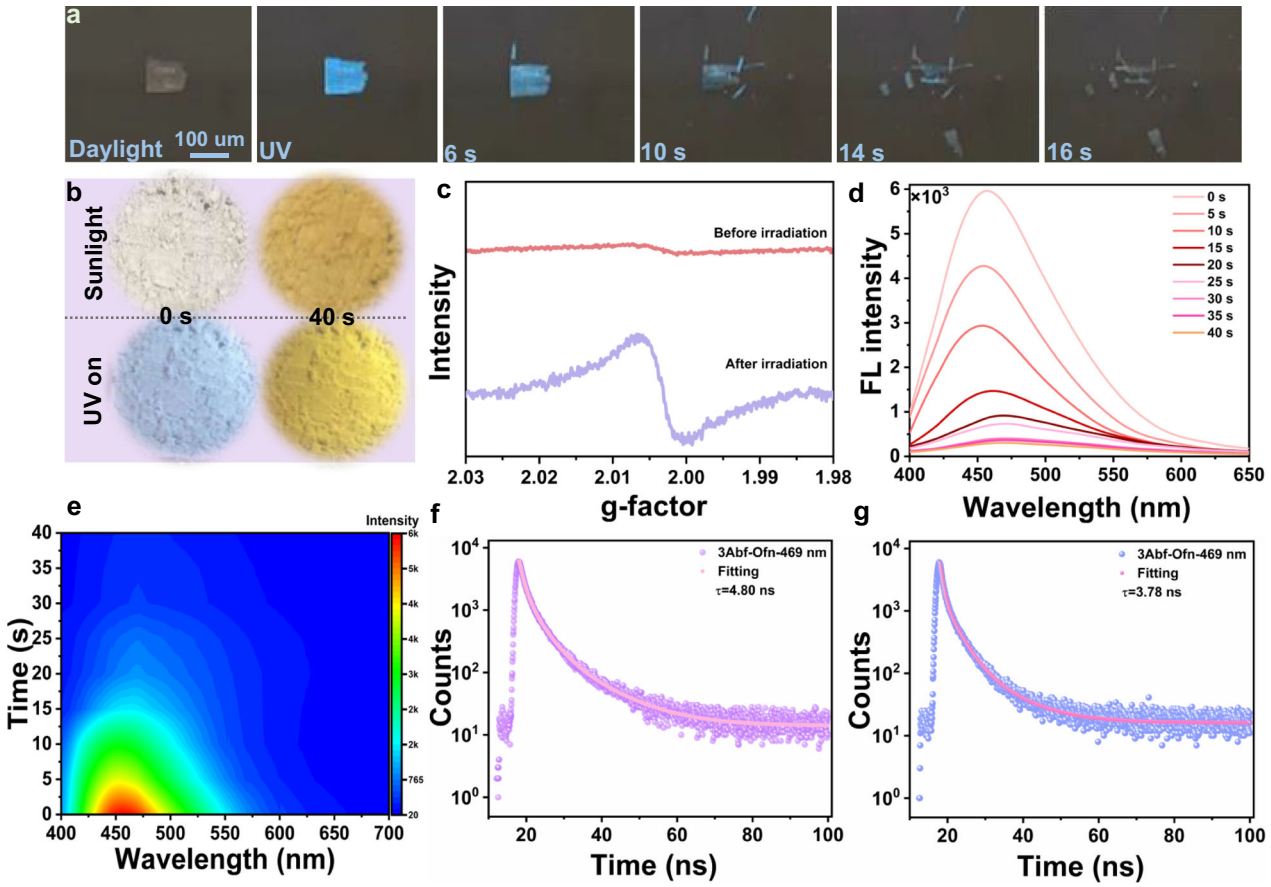

Fig. 3 | Photosalient effects and photochromism of 3Abf-Ofn. a The photographs of light-induced cracking and popping processes for 3Abf-Ofn crystal. **b** The photochromic behavior of 3Abf-Ofn powder. **c** EPR spectra of 3Abf-Ofn before and after UV irradiation. **d** Emission spectra and emission spectra mapping (**e**) at different irradiation time of 3Abf-Ofn. **f** Fluorescence lifetime decay profile of 3Abf-Ofn before UV light irradiation. **g** Fluorescence lifetime decay profile of 3Abf-Ofn after UV light irradiation.

response speeds (Supplementary Fig. 9), which are largely related to various internal and external factors, such as internal defects, crystal size, light intensity, as well as morphology[45–48]. Crucially, thermal effects can be excluded as the primary driver of these responses. Differential scanning calorimetry (DSC) result (Supplementary Fig. 10) indicates that the as-prepared 3Abf-Ofn crystals have a melting point of 139 °C, and no morphological changes are observed when the crystals are heated below this temperature (Supplementary Fig. 11). More importantly, the maximum temperature of the crystals reached about 42 °C under continuous UV irradiation. Therefore, it can be concluded that the mechanical motions and photochromic behavior of 3Abf-Ofn crystals are primarily driven by the direct influence of UV light stimulation rather than thermal-induced structural changes.

Unlike the dynamic mechanical behavior of crystalline 3Abf-Ofn at the macroscopic scale, the powder sample remains static upon UV light irradiation, confirming that the fine particles prevent the accumulation of energy due to size effect[48]. It is worth mentioning that photochromic processes are retained for 3Abf-Ofn powder, with the powder samples transitioning from white to deep yellow rapidly within 20 s (Fig. 3b), accompanied by the emergence of a new absorption band in the scope of 370-450 nm (Supplementary Fig. 12), indicating the formation of light-induced species with radical character. Correspondingly, a pronounced signal with g = 2.004 can be detected for the colored sample after irradiation in electron paramagnetic resonance (EPR) spectra (Fig. 3c), while only a weak signal is observed before irradiation, verifying the generation of free radicals during the light-induced electron transfer process for the visible coloring process. Furthermore, 3Abf-Ofn powder exhibits a distinct decrease in fluorescence intensity upon UV irradiation (Fig. 3d and e), consistent with their decreasing trends in both fluorescence lifetimes from 4.80 to 3.78 ns (Fig. 3f, g) and fluorescence quantum yield (PLQY) (Supplementary Figs.13 and 14). The quenching is attributed to the PET generating a non-emissive radical state[49], as well as the self-absorption effect[50]. This is further supported by the notable spectral overlap between the UV-Vis absorption bands of photoproducts during irradiation and fluorescence emission spectra of the pristine 3Abf-Ofn material. Furthermore, the yellow powder by short-term UV irradiation can be restored to the initial state upon heating to 95 °C (Supplementary Fig. 15). The thermal decomposition as a contributing factor during the fading process can be excluded based on the decomposition temperature of 3Abf-Ofn. Moreover, the PXRD and FT-IR spectra after thermal treatment are nearly in agreement with those before the photochromic process (Supplementary Figs. 16, 17), indicating no significant structural changes during this process. Importantly, the pronounced decrease in EPR signal intensity after heat treatment, suggesting the photogenerated radicals can be quenched, which is directly correlated with the color fading and fluorescence recovery[49,51]. Furthermore, repeated UV irradiation of the thermally treated 3Abf-Ofn samples leads to the reappearance of the EPR signal and a darkening of the sample color (Supplementary Fig. 18), confirming that the color recovery is primarily attributed to the regeneration of photogenerated radicals upon irradiation. However,

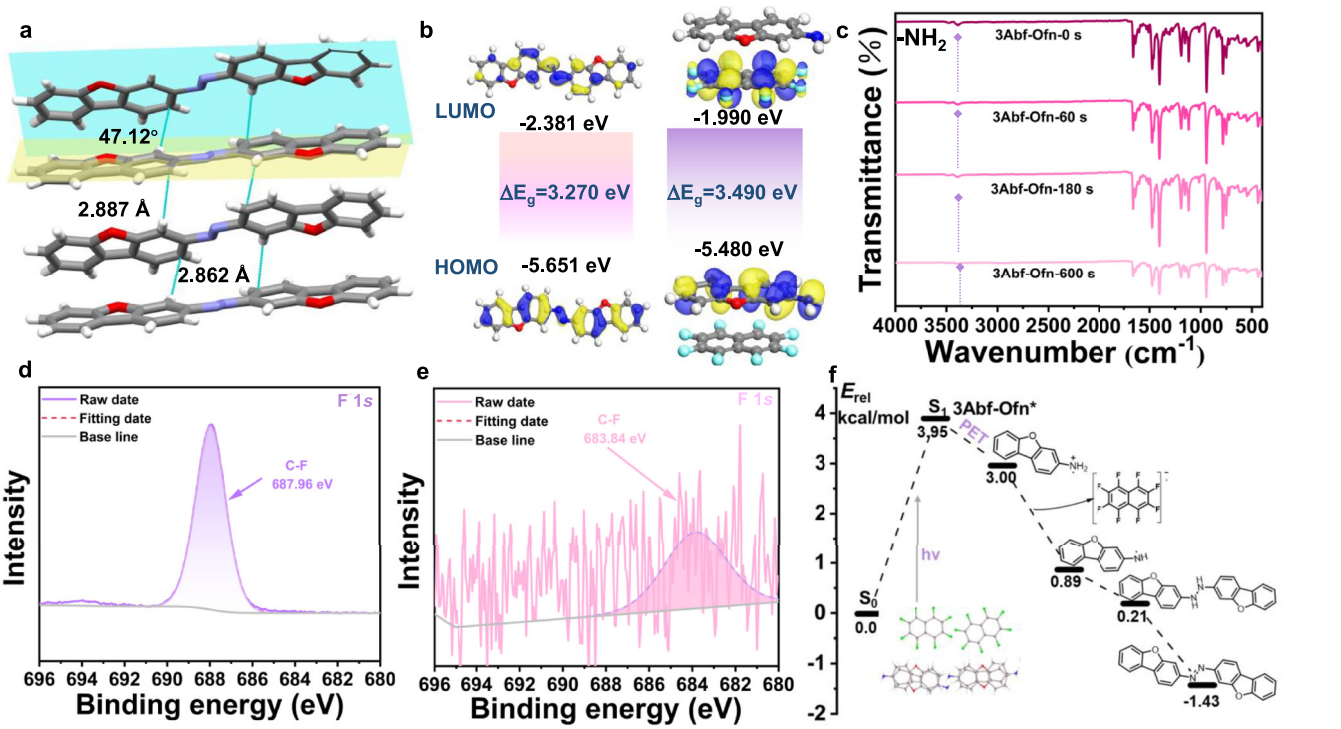

Fig. 4 | The mechanism of photochemical transformation from 3Abf-Ofn to Bfa. **a** C-H···π interactions and dihedral angle of photoproduct Bfa. **b** Calculated energy and molecular orbital diagrams of HOMOs and LUMOs for photoreaction compound Bfa and 3Abf-Ofn, respectively. **c** FT-IR patterns of 3Abf-Ofn sample before and after UV irradiation. **d** High-resolution F 1*s* XPS spectra of 3Abf-Ofn before UV irradiation. **e** High-resolution F 1*s* XPS spectra of 3Abf-Ofn after UV irradiation for 10 min. **f** Energy profile of the reaction by DFT calculations.

following prolonged UV irradiation, the powder undergoes a color darkening upon thermal treatment (Supplementary Fig. 19) and exhibits new diffraction peaks in the PXRD patterns (Supplementary Fig. 20), owing to the active radicals that may trigger side reactions[52]. Meanwhile, the intensity of UV-Vis absorption peaks decreases significantly upon heating, approaching the initial spectral profiles prior to irradiation (Supplementary Fig. 21), indicating the coexistence of the reversible radical-based original reactants and photoproducts in a mixed phase. In contrast, mechanically grinding achieves good cycling stability without altering the crystalline phase, as evidenced by PXRD patterns (Supplementary Fig. 22) that are consistent with those of the light-irradiation product. This structural recovery is accompanied by a significant increase in blue fluorescence intensity observable to the naked eye (Supplementary Fig. 23).

Mechanism investigation for photo-responsive properties

To further clarify the origin of the photochemical reaction process in the 3Abf-Ofn cocrystal during UV light irradiation, various structural characterization techniques were performed. SCXRD, serving as the most direct and powerful tool to determine potential structural changes, was further performed on freshly split crystals maintained in high quality with shorter UV irradiation time. After 20 s of light irradiation, the 3Abf-Ofn crystal exhibits an expansion of approximately 0.25% along the *b*-axis and a contraction of about 0.34% along the *c*-axis. Additionally, the dihedral angle between 3Abf and neighboring Ofn molecules decreases from 6.91°, and 6.86° to 3.76°, and 4.65°, respectively (Supplementary Figs. 24 and 25). This anisotropic lattice deformation indicates that significant relative rotation and structural rearrangement between molecules occur during the photoinduced process, generating and gradually accumulating internal stress within the lattice. However, the crystal quality of 3Abf-Ofn has been significantly deteriorated after sufficient irradiation for 2 h, making it difficult to resolve photochemical reaction products by single-crystal X-ray diffraction. After numerous attempts[10,14,53–55], the final photoproduct can be obtained successfully through solution recrystallization and confirmed the formation of only Bfa.

The photoreaction compound Bfa is crystallized in the monoclinic space group $P2_1/c$, as summarized in Supplementary Table 1. The adjacent Bfa molecules are tightly connected through strong C-H···π interactions (2.862 and 2.887 Å), with a dihedral angle of 47.12°, forming an ordered network structure along the b axis (Fig. 4a, and Supplementary Fig. 26). The highest occupied molecular orbital (HOMO) and the lowest unoccupied molecular orbital (LUMO) of Bfa are predominantly distributed across the conjugated backbone. The calculated energy gap of Bfa (3.270 eV) is lower than that of the 3Abf-Ofn molecules (3.490 eV) (Fig. 4b), further corresponding to experimental evidence demonstrating the visible light absorption capacity of the 3Abf-Ofn under continuous illumination. In addition, the intensity of the peak at 5.5 ppm in ^{1}H NMR spectra exhibit a significant change following UV light irradiation, indicating an alteration in the chemical environment of the hydrogen atoms of -NH_2 (Supplementary Fig. 27). In the FT-IR spectra, the intensity of -NH_2 stretching vibration peak at 3388 cm^{-1} gradually weakens upon prolonged UV irradiation time (Fig. 4c, and Supplementary Fig. 28), suggesting a change in the content of -NH_2 groups and involvement in the photochemical transformation. Furthermore, new diffraction peaks appear in the PXRD pattern (Supplementary Fig. 29), which correspond well to the simulated pattern of the Bfa product. High-resolution mass spectrometry (HRMS) further confirms the formation of the final product Bfa ($C_{24}H_{14}N_2O_2$), with a detected m/z value of 363.111 matching the calculated exact mass. Moreover, the relative abundance of Bfa markedly increases from 20% to nearly 100% upon continuous irradiation for 2 h (Supplementary Fig. 30). Subsequent X-ray photoelectron

spectroscopy (XPS) analysis reveals that the signal intensity of the C-F bond diminishes with increasing UV irradiation time (Fig. 4d, e, Supplementary Figs. 31 and 32), consistent with the release of Ofn during photoinduced process, which contributes to the stability of the photoproduct Bfa.

To elucidate the reaction pathway from 3Abf-Ofn to Bfa, the control experiments with alternative electron donors (1-aminodibenzofuran (1Abf) and 2-aminodibenzofuran (2Abf)) and acceptors (1,2,4,5-Tetracyanobenzene (Tcnb), 3,4,5,6-Tetrafluorophthalonitrile (Tfpn), and 3,4,5,6-Tetrachlorophthalonitrile (Tcpn)) under identical conditions are conducted. Bfa compounds can be detected (m/z 363.111) by HRMS upon UV irradiation of 1Abf–Ofn (Supplementary Fig. 33) and 2Abf–Ofn (Supplementary Fig. 34), which demonstrate that the strategy can be extended to more systems. EPR results of 1Abf–Ofn and 2Abf–Ofn reveal the presence of radical signals by PET, accompanied by photochromic behaviors (Supplementary Figs. 35–37). Notably, the reaction proceeds efficiently even under a nitrogen atmosphere, as evidenced by both Bfa product formation (Supplementary Fig. 38) and photochromic behavior (Supplementary Fig. 39), confirming that this reaction is not a conventional oxidative coupling pathway with molecular oxygen[56,57]. However, it is failed to observe color changes and yield azo compounds in 3Abf-Tcnb, 3Abf-Tfpn and 3Abf-Tcpn (Supplementary Fig. 40), underscoring the crucial role of Ofn in driving the reaction. Based on the experimental findings, we propose the reaction mechanism. Upon UV irradiation, photoinduced electron transfer from the electron-donor 3Abf to the electron-acceptor Ofn generates radicals, which subsequently undergo intermolecular N–N coupling to form the azobenzene derivative Bfa. Density functional theory (DFT) calculations (Fig. 4f) are performed to support our proposed reaction pathway. Upon photoexcitation, 3Abf-Ofn enters the singlet excited state, followed by intermolecular electron transfer to generate radical species. Subsequently, the -NH2•+ of 3Abf deprotonates to form -NH•, resulting in a reduction of the system energy to 0.89 kcal/mol. The generated radical then participates in N–N coupling process to yield an azo-linked dimer, and final product energy (1.43 kcal/mol) is lower than the initial state, demonstrating that PET-assisted coupling reaction of 3Abf-Ofn is thermodynamically favorable.

The photochemical reactivity of the 3Abf–Ofn cocrystal is intrinsically linked to its macroscopic photomechanical response. To further uncover the origin behind the photoinduced mechanical motion, taking the pristine 3Abf and 3Abf-Tcpn cocrystal systems as an example. Under identical irradiation conditions, both pristine 3Abf and 3Abf-Tcpn cocrystals remain stable macroscopic morphologies (Supplementary Figs. 5 and 41), and their photoresponse properties are distinctly different from those of the 3Abf-Ofn system (Supplementary Figs. 42 and 43). SCXRD analysis further reveals the self-assembly patterns and intermolecular interactions are key factors influencing photochemical processes. Pure 3Abf adopts a classic herringbone packing motif driven by C–H···π interactions (Supplementary Fig. 44a), the closest N···N distance is as long as 7.312 Å (Supplementary Fig. 44b), indicating molecules struggle to achieve close-range cooperative motion through slip or rotation, preventing observable macroscopic deformation. The 3Abf-Tcpn cocrystals present D-A arrangement pattern (Supplementary Fig. 45), but its structure is stabilized by hydrogen bonds interactions (N-H···N, C-H···N, and N-H···F) that form rigid dimers units (Supplementary Fig. 46), which further assemble into highly parallel, tightly packed DADA columns. This strong hydrogen-bonding network rigidly locks molecular conformation and significantly restricts the degrees of freedom for molecular motion in the excited state. For the as-prepared 3Abf-Ofn crystals, intermolecular interactions are dominated by weak interactions (C–F···H, F···F and π-π) contacts, lacking strong directional hydrogen bond constraints between 3Abf and Ofn. This packing arrangement displays a loosely packed character, leading to localized structural instability. Upon light stimulation, energy is rapidly transferred, inducing swift molecular twisting in these disordered regions, thereby initiating a drastic phase transition. During the phase transition, the extreme proximity of adjacent 3Abf units facilitates a radical coupling reaction. Meanwhile, Ofn is no longer stabilized within the lattice due to loss of structural compatibility. Given its low melting point and high vapor pressure[58], Ofn readily sublimes even at room temperature, thus facilitating its escape through sublimation as the temperature increases under UV irradiation. When the accumulated internal stress is abruptly released, the crystal lattice is broken, giving rise to observable mechanical effects that ultimately lead to an amorphous state, marking the transformation from a metastable to a stable state[13,46]. For the localized plastic deformation observed in a few samples, which can be attributed to a relatively gradual stress release that does not reach the energy threshold necessary to induce brittle fracture. At the microscopic level, this behavior originates from sudden anisotropic changes in the unit cell[48]. The molecular rearrangements of 3Abf-Ofn at transition states cause lattice volume expansion, which can reach up to 84.8% (from 909.01 to 1679.84 $Å^3$). The anisotropic expansion of the crystal occurs rapidly to drive macroscopic motion. Importantly, the structural defect environment formed by molecular disordering, to some extent, facilitates molecular rearrangement, thereby creating favorable conditions for the photo-induced mechanical response.

Photophysical properties for 3Abf-Ofn doped into PMMA film

Considering the excellent photoresponsive properties of the 3Abf–Ofn cocrystals and the practical requirements for processability and integrability of solid-state functional materials, we incorporated 3Abf-Ofn powder into polymethyl methacrylate (PMMA) polymer matrices in dichloromethane to improve their overall applicability. The PXRD analysis indicate that 3Abf-Ofn components are effectively doped into the PMMA forming amorphous states, with no significant phase separation (Fig. 5a). XPS demonstrates the different functional groups between 3Abf-Ofn and the PMMA matrix (Supplementary Figs. 47 and 48). Furthermore, the 3Abf-Ofn@PMMA film shows distinctive optical characteristics, in addition to preserving the photochromism (Supplementary Fig. 49) of the pristine 3Abf-Ofn powder. Specifically, the initial fluorescence signal is weak, however, the fluorescence intensity increases by approximately 10-fold after continuous irradiation for 20 s (Fig. 5b and c), and fluorescence lifetime slightly increases from 3.93 ns to 4.00 ns (Supplementary Fig. 50), revealing a clear phenomenon of photoactivated fluorescence enhancement. The behavior can be attributed to the intrinsic aggregation-induced emission (AIE) of 3Abf-Ofn (Supplementary Fig. 51) and UV-induced transient polymer chain mobility, facilitating molecular ordered aggregates collectively[6,59–61]. Interestingly, when different wavelengths of visible light are employed as excitation sources, the 3Abf-Ofn@PMMA film displays pronounced EWDE (Fig. 5d), with the wavelengths of emission spectra spanning from 450 nm to 680 nm, corresponding their CIE coordinates from the blue to the red region (Supplementary Fig. 52), indicating a broad tunability in luminescence, which exhibit promising applications in smart displays, multicolor fluorescent devices, and optical encoding technologies. Upon prolonged UV irradiation, a significant reduction in fluorescence intensity is observed for 3Abf-Ofn@PMMA film (Fig. 5e), with the PLQY decreasing from 4.32% to 3.90% (Supplementary Fig. 53). The fluorescence attenuation is attributed to photochromism induced by radical formation, as evidenced by enhanced visible-light absorption (Fig. 5f) and increase in EPR signal intensity (Supplementary Fig. 54). Additionally, the 1Abf molecules are isostructural systems of 3Abf. 1Abf–Ofn powder exhibits photophysical properties analogous to those of 3Abf–Ofn (Supplementary Figs. 55–59). Correspondingly, the 1Abf-Ofn@PMMA films also show

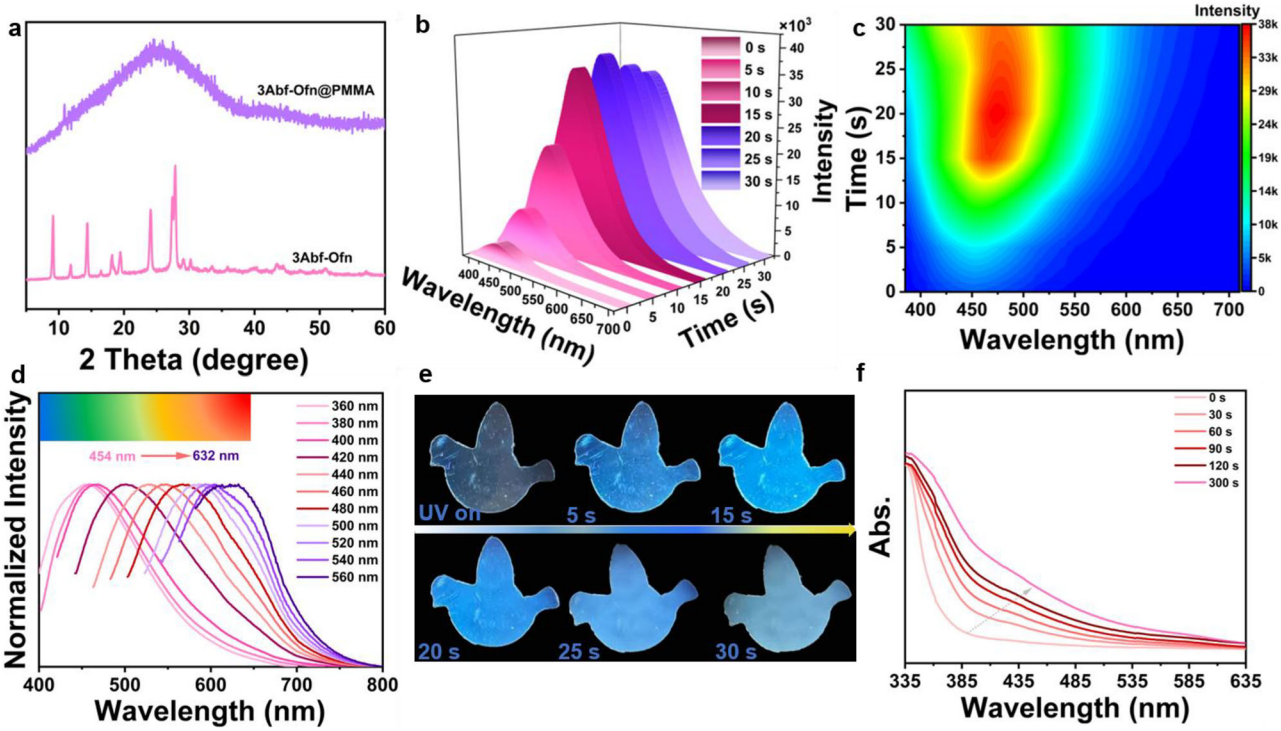

Fig. 5 | Photophysical properties for 3Abf-Ofn@PMMA. a PXRD patterns of 3Abf-Ofn powder and 3Abf-Ofn@PMMA film. **b** PL emission spectra and (**c**) emission spectra mapping of 3Abf-Ofn@PMMA film under UV irradiation. **d** Emission spectra and of 3Abf-Ofn@PMMA film under different excitation wavelengths. **e** Photographs of light-induced fluorescence enhancement processes for 3Abf-Ofn@PMMA film. **f** UV-Vis spectra of 3Abf-Ofn@PMMA at different irradiation time.

photoactivated fluorescence enhancement effect followed by quenching upon prolonged irradiation, as well as EWDE (Supplementary Figs. 60–63). In contrast, neither significant fluorescence enhancement nor EWDE is detected in 3Abf-Tcpn@PMMA and 3Abf@PMMA films, and the overall fluorescence intensity is weak, respectively (Supplementary Figs. 64-66). Supplementary Figs. 67–69 clearly indicate that the photoresponse properties of films are related to the inherent optical properties of the dopant molecules themselves. Replacing the PMMA matrix with polyvinyl alcohol (PVA) matrix in aqueous solution, both 3Abf-Ofn@PVA film and 1Abf-Ofn@PVA film display only conventional photochromic behavior, with a narrower excitation-dependent emission range (Supplementary Figs. 70–74). XPS spectra of 3Abf-Ofn@PVA show the presence of C-O-C and C-O-H bonding signals at 533.38, and 532.35 eV, respectively (Supplementary Fig. 75). The strong bonding interactions restrict molecular flexibility and promote fewer emissive states. Furthermore, we further fabricated 3Abf-Ofn doped films using other polymer matrices, including polylactic acid (PLA), polyamide (PA), and polyvinylpyrrolidone (PVP) in dichloromethane. The results reveal that similar light-regulating behavior (Supplementary Figs. 76–80) to that in 3Abf–Ofn@PMMA film, demonstrating that the photoactivated aggregation induced luminescence mechanism exhibits excellent reproducibility in various hydrophobic polymer matrices.

Applications

Based on tri-state fluorescence switching in 3Abf-Ofn@PMMA film materials, the potential applications in multi-level anti-counterfeiting and information encryption are investigated. As illustrated in Fig. 6a, peace dove and heart-shaped masks are placed on 3Abf-Ofn@PMMA film samples. Before UV irradiation, the film remains transparent with no visible patterns under both daylight and UV light, demonstrating excellent properties for information storage. By applying UV irradiation of varying durations to different regions, multi-level and programmable optical responses can be achieved. For instance, after a 5 s irradiation of the heart region, no noticeable changes are observed under daylight. However, due to

UV light-induced fluorescence enhancement effect of 3Abf-Ofn@PMMA film, this region exhibits clear and bright blue fluorescence, forming a time-resolved fluorescence intensity anti-counterfeiting mark. Meanwhile, the use of excitation light sources at different wavelengths enables multi-channel optical responses, providing an additional security dimension for information encryption and significantly enhancing confidentiality. When the peace dove region is exposed to UV light for a longer time, a significant photochromic response occurs, resulting in a visible color contrast under natural light. The entire film is exposed to 20 s of UV light, which falls in the fluorescence enhancement response window. Under these conditions, the localized fluorescence signal in the heart region is gradually masked by the enhanced background fluorescence, effectively concealing and fading the first-level information. Upon further prolonging the UV exposure, the peace dove pattern gradually fades, ultimately erasing the information and enabling a system reset. Furthermore, the fluorescent visualization properties of 3Abf-Ofn@PMMA can be applied in digital information encryption system (Fig. 6b). The correct password 3113 is only revealed under fluorescent mode after UV irradiation 20 s. In contrast, the initial mask encoding is 1331, which is clearly visible under daylight and serves as misleading surface-level information. Authorized personnel can retrieve the true password 3113 via fluorescent imaging under UV illumination after the designated exposure time. Continued irradiation for 240 s induces fluorescence saturation across the entire area, transitioning the display to 8888, an interference pattern designed to prevent unauthorized access. Moreover, the photochromic materials 3Abf-Ofn and 1Abf-Ofn can be extended to functional decorative applications by embedding them into a mold (Fig. 6c and

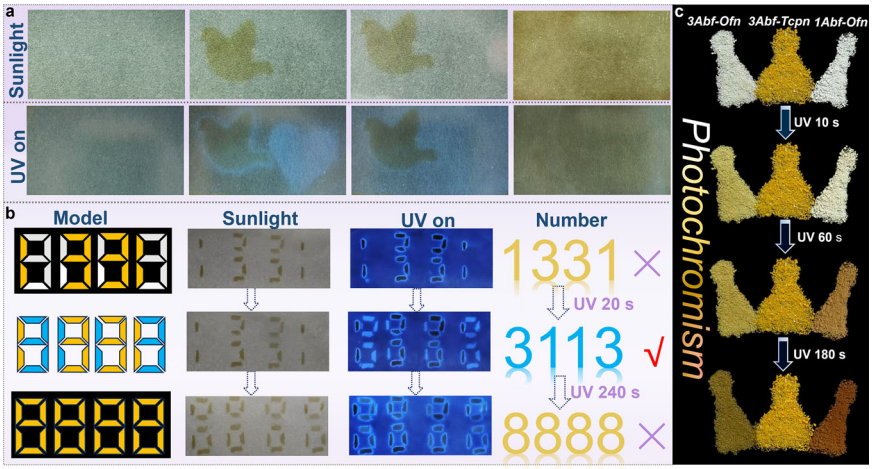

Fig. 6 | Applications. a Information anti-counterfeiting of 3Abf-Ofn@PMMA film. **b** Digital encryption of 3Abf-Ofn@PMMA film. **c** Functional decorative of 3Abf-based and 1Abf-Ofn powder.

Supplementary Fig. 81). Under UV irradiation, 3Abf-Ofn changes from white to yellow, while 1Abf-Ofn turns brown. With prolonged UV illumination, 3Abf-Ofn and 1Abf-Ofn powders exhibit a noticeable color gradient, showing excellent visual appeal. Importantly, the colors can be restored to their initial states through mechanical pressure, enabling reversible color switching.

Discussion

In summary, we reported an innovative design strategy for constructing multifunctional light-responsive crystalline materials through cocrystal self-assembly and photochemical reaction mechanisms, enabling the regulation of static optical responses and dynamic mechanical responses. The 3Abf–Ofn cocrystal exhibits distinct photochromic properties, which essentially originate from radicals generated via the PET process, further triggering intermolecular N-N coupling to form Bfa, accompanied by the release of volatile Ofn. The reaction process relieves internal lattice stress and thereby drives macroscopic photomechanical motions. Furthermore, 3Abf-Ofn@PMMA film exhibits a sequential modulation process from light-induced fluorescence enhancement and EWDE to photochromic cascade, offering a viable platform for spatiotemporally encoded information encryption, multi-level security labeling, and anti-counterfeiting technologies. This study establishes a viable photochemical synthetic route for the preparation of azobenzene derivatives, laying an important insight and theoretical foundation for the development of intelligent light-responsive functional materials.

Methods

Materials

3-Aminodibenzofuran (3Abf, 98%), 1-Aminodibenzofuran (1Abf, 98%), 2-Aminodibenzofuran (2Abf, 98%), Octafluoronaphthalene (Ofn, 96%), 1,2,4,5-Tetracyanobenzene (Tcnb, 97%), 3,4,5,6-Tetrafluorophthalonitrile (Tfpn, 98%), and 3,4,5,6-Tetrachlorophthalonitrile (Tcpn, 98%) were purchased from commercial suppliers (Aladdin and TCI) and used without further purification.

Preparation of 3Abf-based cocrystals. In typical processes, the 3Abf-Ofn, and 3Abf-Tcpn cocrystals were obtained by slow evaporation in a methanol/dichloromethane solution (v/v = 1:1, 30 mL) with the initial molar ratios of the two compositions in 1:1. The single crystals can be obtained within 10-15 days.

Preparation of PMMA, PLA, PA, and PVP films. 20 mg 3Abf, 20 mg 3Abf-Ofn, 20 mg 3Abf-Tcpn, and 20 mg 1Abf-Ofn powder were thoroughly mixed with polymer-dichloromethane solution, respectively, and then stirred the resulting mixture for 30 min to ensure uniform homogeneity. Following vigorous stirring, the well-mixed mixture solution was directly deposited onto a clean substrate and allowed to evaporate slowly to form uniform films.

Preparation of PVA film. 20 mg 3Abf-Ofn, 20 mg 1Abf-Ofn powder, and 500 mg PVA polymer were thoroughly added into a 10 mL water solution, respectively, and then stirred and heated the resulting mixture at 80 °C for at least 12 h to ensure uniform homogeneity. After vigorous stirring, the homogenously mixed solution was directly deposited onto a clean substrate and allowed to evaporate slowly to form uniform films.

Computational details

The density functional theory (DFT) calculations were performed using the Gaussian 16 program package. All geometric optimizations and energy calculations were carried out with the m062x hybrid functional, combined with the 6-311 + +g (d,p) basis set, containing the solvent(dichloromethane)effect modeled with the solvation model of density (SMD)method. Vibrational frequency analyses were performed to verify that all optimized geometries correspond to energy minima, free of imaginary frequencies. For accelerating the self-consistent field (SCF) convergence and improving calculation efficiency, the extra-quick convergence (XQC) algorithm was adopted (controlled by the SCF = XQC keyword). All structures were optimized until the convergence criteria for geometries and energies were fully satisfied.

Characterizations

PXRD pattern were performed on X-ray diffractometer (Rigaku, 18 kW/D/Max2550VB/PC, Cu Kα radiation, λ = 1.5418 Å, 40 kV/100 mA power) at room temperature. SCXRD data were collected on a Bruker APEX-II CCD diffractometer with Cu Kα radiation (λ = 1.54178 Å) at 298 K, and the structures were solved with Olex2. FT-IR were measured using the WQF-530 instrument. UV-Vis absorption spectra were taken using Shimadzu UV2700 (Japan). ^{1}H NMR spectra were obtained using a Bruker 500 MHz Spectrometer. EPR was measured with a JES-320 JEOL RESONANCE system (microwave 9.422 GHz). XPS measurements were performed at the Thermo Scientific K-Alpha (America) at the SLS. FL

spectra were characterized using a Shimadzu RF-6000 instrument. HRMS is collected on a Thermo Scientific Q Exactive Orbitrap. The photoluminescence lifetime (τ) and photoluminescence quantum yield (PLQY) were measured on an Edinburgh FLS1000 spectrometer. TGA/DSC analyses were obtained using a Rigaku, with the rate of 10 °C/min in flowing nitrogen. Crystal morphology modelling and corresponding Miller indices of dominant faces are predicted through the Bravais–Friedel Donnay-Hulme (BFDH) method in the Mercury software based on single crystal XRD data.

Data availability

The authors declare that the data in this study are available in this article and the supplementary information files and available from the corresponding authors on request. The crystallographic data for the structures reported in this article have been deposited with the Cambridge Crystallographic Data Centre (CCDC) as deposition numbers 2479066 (3Abf-Ofn), 2479067 (Bfa), and 2479133 (Abf-Tcpn). These data can be obtained free of charge via www.ccdc.cam.ac.uk/data_request/cif. Atomic coordinates of the optimized computational models. Source data are provided with this paper.

References

1. Awad, W. M. et al. Mechanical properties and peculiarities of molecular crystals. *Chem. Soc. Rev.* **52**, 3098–3169 (2023).
2. Terao, F. et al. Light-driven molecular-crystal actuators: rapid and reversible bending of rodlike mixed crystals of diarylethene derivatives. *Angew. Chem. Int. Ed.* **51**, 901–904 (2012).
3. Garcia-Garibay, M. A. Molecular crystals on the move: from single-crystal-to-single-crystal photoreactions to molecular machinery. *Angew. Chem. Int. Ed.* **46**, 8945–8947 (2007).
4. Moulin, E. et al. From molecular machines to stimuli-responsive materials. *Adv. Mater.* **32**, 1906036 (2019).
5. Hayashi, S. et al. Anisotropic poisson's effect and deformation-induced fluorescence change of elastic 9,10-dibromoanthrathene single. *Crystals. Angew. Chem. Int. Ed.* **59**, 16195–16201 (2020).
6. Wang, J. J. et al. Dynamic mechanoresponsive polymers enabled by ring-opening polymerization of cyclic propargyl carbonates. *Chem* 102643, https://doi.org/10.1016/j.chempr.2025.102643 (2025).
7. Ding, Y. et al. Synergistic Covalently and Mechanically Interlocked Polymer. *Angew. Chem. Int. Ed.* e202510140, 10.1002/anie.202510140 (2025).
8. Wang, M. et al. Vapochromic behaviors of a solid-state supramolecular polymer based on exo-wall complexation of perethylated pillar [5] arene with 1,2,4,5-tetracyanobenzene. *Angew. Chem. Int. Ed* **60**, 8115–8120 (2021).
9. Yang, X. et al. Cryogenically flexible phosphorescent organic crystals that transmit self-sustained persistent luminescence with spatiotemporal control. *J. Am. Chem. Soc.* **147**, 22961–22971 (2025).
10. Li, S. et al. Manipulating light-induced dynamic macro-movement and static photonic properties within 1d isostructural hydrogen-bonded molecular cocrystals. *Angew. Chem. Int. Ed* **59**, 22623–22630 (2020).
11. Li, S. et al. Tuning light-driven motion and bending in macroscale-flexible molecular crystals based on a cocrystal approach. *ACS Appl. Mater. Inter.* **10**, 22703–22710 (2018).
12. Peng, J. et al. Mechanical effects of elastic crystals driven by natural sunlight and force. *Angew. Chem. Int. Ed.* **62**, e202311348 (2023).
13. Xu, T. et al. Engineering photomechanical molecular crystals to achieve extraordinary expansion based on solid-state [2+2] photocycloaddition. *J. Am. Chem. Soc.* **144**, 6278–6290 (2022).
14. Li, W. et al. Photochemical reaction front propagation and control in molecular crystals. *J. Am. Chem. Soc.* **146**, 32757–32765 (2024).
15. Xing, C. et al. Solid-state photochemical cascade process boosting smart ultralong room-temperature phosphorescence in bismuth halides. *Angew. Chem. Int. Ed.* **63**, e202402634 (2024).
16. Bushuyev, O. S. et al. Fast, reversible, and general photomechanical motion in single crystals of various azo compounds using visible light. *Adv. Mater.* **25**, 1796–1800 (2013).
17. Zhou, B. et al. Recent advances of dynamic molecular crystals with light-triggered macro-movements. *Appl. Phys. Rev.* **8**, 041310 (2021).
18. Naumov, P. et al. Dynamic single crystals: kinematic analysis of photoinduced crystal jumping (the photosalient effect). *Angew. Chem. Int. Ed.* **52**, 1–7 (2013).
19. Bhandary, S. et al. Single-crystal-to-single-crystal photosynthesis of supramolecular organoboron polymers with dynamic effects. *J. Am. Chem. Soc.* **146**, 8659–8667 (2024).
20. Samanta, R. et al. Mechanical actuation and patterning of rewritable crystalline monomer– polymer heterostructures via topochemical polymerization in a dual-responsive photochromic organic material. *ACS Appl. Mater. Inter.* **12**, 16856–16863 (2020).
21. Liao, P. et al. Radical-induced photochromic silver (i) metal–organic frameworks: alternative topology, dynamic photoluminescence and efficient photothermal conversion modulated by anionic guests. *Angew. Chem. Int. Ed* **63**, e202401448 (2024).
22. Zhao, Z. et al. Photochromic luminescence of organic crystals arising from subtle molecular rearrangement. *Nat. Commun.* **15**, 5054 (2024).
23. Thaggard, G. C. et al. Switching from Molecules to Functional Materials: Breakthroughs in Photochromism with MOFs. *Adv. Mater.* 2410067 (2024).
24. Hassan, F. et al. Photochromic carbon nanomaterials: an emerging class of light-driven hybrid functional materials. *Adv. Mater.* **36**, 2401912 (2024).
25. Li, X. et al. A reversible photochromic covalent organic framework. *Nat. Commun.* **15**, 8484 (2024).
26. Shao, J. et al. Promising coloration composite strategy to multicolor photochromism for on-demand information displays. *Adv. Funct. Mater.* **35**, 2425059 (2025).
27. Zi, Y. et al. Force-light-heat stimulation-induced multicolor chromism and multifunctional applications of europium tungstate phosphor. *Nat. Commun.* **16**, 6857 (2025).
28. Xiao, Y. et al. 3D Printable materials with visible light triggered photochromism and room temperature phosphorescence. *J. Am. Chem. Soc.* **147**, 20372–20380 (2025).
29. Tian, Q. et al. Dynamic regulation of radical photochromism and photoluminescence via polymer polarity. *Angew. Chem. Int. Ed.* e202509506 (2025).
30. Xiao, Y. et al. Thermally activated photochromism: realizing temperature-gated triphenylethylene photochromic materials. *Adv. Funct. Mater.* **34**, 2312930 (2024).
31. Zhu, M. et al. Advanced functional photochromic wearables with superior durability and stability for sustainable applications. *Adv. Funct. Mater.* **34**, 2406840 (2024).
32. Sun, L. et al. Thermally activated delayed fluorescence in an organic cocrystal: narrowing the singlet-triplet energy gap via charge transfer. *Angew. Chem. Int. Ed.* **58**, 11311–11316 (2019).
33. Xu, J. et al. Visible light-responsive crystalline b←n host adducts with solvent-induced allosteric effect for guest release. *Angew. Chem. Int. Ed.* **63**, e202411880 (2024).
34. Ren, S. et al. A relay-type solid-state macrocyclic host–guest system for selective isomer adsorption, controlled release, and turn-on colorimetric sensing of 1-/2-bromoalkanes. *Adv. Mater.* **37**, 2504417 (2025).

35. Cui, J. et al. Efficient shortwave infrared photodetection through polymer: cocrystal blend film-based field-effect transistors. *Adv. Opt. Mater.* **13**, 2403275 (2025).
36. Ren, S., Qiao, G.-Y. & Wu, J.-R. Supramolecular-macrocycle-based functional organic cocrystals. *Chem. Soc. Rev.* **53**, 10312–10334 (2024).
37. Mantel, G. C. et al. Effect of chirality on ultrafast triplet exciton formation in electron donor-acceptor cocrystals. *J. Am. Chem. Soc.* **147**, 29592–29601 (2025).
38. Zhu, L. et al. Triethylamine vapor-induced cyclization reaction in cocrystals leading to cocrystal-to-polycrystal transformation. *Nat. Commun.* **16**, 6441 (2025).
39. He, X. et al. Recent advances in tunable solid-state emission based on α-cyanodiarylethenes: from molecular packing regulation to functional development. *Chem. Soc. Rev.* **53**, 6636–6653 (2024).
40. Ren, S. et al. Geminiarene-based charge-transfer cocrystals with dichromatic variants and stimuli-responsive structural interconversion. *Angew. Chem. Int. Ed.* **64**, e202506549 (2025).
41. Wang, X. et al. Recent advances of organic cocrystals in emerging cutting-edge properties and applications. *Angew. Chem. Int. Ed.* **63**, e202416181 (2024).
42. Borchers, T. H. et al. Three-in-one: dye-volatile cocrystals exhibiting intensity-dependent photochromic, photomechanical, and photocarving response. *J. Am. Chem. Soc.* **145**, 24636–24647 (2023).
43. Li, S. et al. Manipulating dynamic light-driven solid-liquid transition and static reversible photochromism by an organic cocrystal strategy. *Angew. Chem. Int. Ed.* **64**, e202500238 (2025).
44. Palmer, J. R. et al. Molecular cocrystal packing suppresses hopping-driven decoherence of excitonic spin qubits. *J. Am. Chem. Soc.* **147**, 17394–17403 (2025).
45. Wang, L. et al. Luminescent chromism of boron diketonate crystals: distinct responses to different stresses. *Adv. Mater.* **27**, 2918–2922 (2015).
46. Bhandary, S. et al. Photomechanical motions in organoboron-based phosphorescent molecular crystals driven by a crystal-state [2+2] cycloaddition reaction. *J. Am. Chem. Soc.* **144**, 22051–22058 (2022).
47. Yuhara, K. et al. The photosalient effect and thermochromic luminescence based on o-carborane-assisted π-stacking in the crystalline state. *Angew. Chem. Int. Ed.* **63**, e202319712 (2024).
48. Naumov, P. et al. Mechanically responsive molecular crystals. *Chem. Rev.* **115**, 12440–12490 (2015).
49. Xu, X. et al. Rapidly generated, ultra-stable, and switchable photoinduced radicals: a solid-state photochromic paradigm for reusable paper light-writing. *Angew. Chem. Int. Ed.* **64**, e202422856 (2025).
50. Nie, F. et al. Zero-dimensional halide hybrid bulk glass exhibiting reversible photochromic ultralong phosphorescence. *Nat. Commun.* **15**, 5519 (2024).
51. Huang, Y. et al. Photoinduced π-Bond breakage causing dynamic closing-opening shell transition of Z-type Diphenylmaleonitriles molecules. *Nat Commun* **15**, 6514 (2024).
52. Ding, Y. et al. Tuned intra-and intermolecular photoreactions of tridentate cyanostilbenes with distinct aggregated-state photomechanical and dispersed-state photochromic behaviors. *Adv. Funct. Mater.* **33**, 2212886 (2023).
53. Konieczny, K. A. et al. Topochemical synthesis, micro-electron diffraction (3d ed), and electron beam-initiated topotactic dimer splitting of cis, syn-thymine dimer crystals. *J. Am. Chem. Soc.* **147**, 20426–20430 (2025).
54. Medishetty, R. et al. Single crystals popping under UV light: a photosalient effect triggered by a [2+2] cycloaddition reaction. *Angew. Chem. Int. Ed.* **53**, 5907–5911 (2014).
55. Wang, H. et al. Bending, curling, rolling, and salient behavior of molecular crystals driven by [2+2] cycloaddition of a styrylbenzoxazole derivative. *Angew. Chem. Int. Ed.* **129**, 9591–9595 (2017).
56. Wang, Z. he et al. Mo2C-derived molybdenum oxycarbides afford controllable oxidation of anilines to azobenzenes and azoxybenzenes. *Green Chem* **27**, 3091–3098 (2025).
57. Dutta, B. et al. Mesoporous manganese oxide catalyzed aerobic oxidative coupling of anilines to aromatic azo compounds. *Angew. Chem.* **128**, 2211–2215 (2016).
58. Ye, X. et al. 1D versus 2D cocrystals growth via microspacing in-air sublimation. *Nat. Commun.* **10**, 761 (2019).
59. Shi, Y. et al. Achieving swift and distinct luminescent modulation through manipulating molecular motion in polymers. *Adv. Funct. Mater.* **34**, 2411584 (2024).
60. Wang, Q. et al. Integrating three-primary-color and white long-lasting afterglows in triphenylene-doped polymers for time/space-resolved applications. *Chem. Eng. J.* **507**, 160535 (2025).
61. Ma, Y.-J. et al. A photoinduced electron-transfer strategy for switchable fluorescence and phosphorescence in lanthanide-based coordination polymers. *Chem. Sci.* **15**, 17642–17651 (2024).

Acknowledgements

This study was financially supported by the National Natural Science Foundation of China (No. 22205057, S.L.), the China Postdoctoral Science Foundation (No.2025M770983, S.L.), the Excellent Youth Talent Project of Henan University of Technology (No.21421356, S.L.), the Youth Backbone Teachers of Henan University of Technology (No.21421252, S.L.), the Doctoral Scientific Research Start-up Foundation from Henan University of Technology (No.2021BS055, S.L.), and College Students' Innovation and Entrepreneurial Training Plan Program (No.22420287, S.L.). We thank Shiyanjia Lab (www.shiyanjia.com) for materials characterizations. We also thank Dr. Yuntao Xia and Dr.Xiaoyu Fang for the discussion on the coupling reaction and guest release process, respectively.

Author contributions

S.L. and X.C. conceived the study. S.L. wrote and revised the manuscript. M.X., X.X., W.H., and H.Z. performed the experiments. S.L. and M.X. analyzed the experiments. All authors discussed the results and commented on the manuscript.

Competing interests

The authors declare no competing interests.

Additional information

Supplementary information The online version contains supplementary material available at https://doi.org/10.1038/s41467-026-69434-9.

Correspondence and requests for materials should be addressed to Shuzhen Li or Xiaoyu Cao.

Peer review information *Nature Communications* thanks Ajiaz Dar, Jia-Rui Wu, and the other, anonymous, reviewer for their contribution to the peer review of this work. A peer review file is available.